Journal of Pharmaceutical Analysis 14 (2024) 100911

Contents lists available at ScienceDirect

Journal of Pharmaceutical Analysis

journal homepage: www.elsevier.com/locate/jpa

Original article

Alginate oligosaccharide-mediated butyrate-HIF-1α axis improves skin aging in mice

Ting Gao, Yixuan Li, Xiaoyu Wang, Fazheng Ren*

Department of Nutrition and Health, College of Veterinary Medicine, China Agricultural University, Beijing, 100083, China

ARTICLE INFO

Article history:
Received 7 July 2023
Received in revised form
21 November 2023
Accepted 4 December 2023
Available online 8 December 2023

Keywords:
Alginate oligosaccharide
Skin aging
Butyrate
HIF-1α
Mitophagy

ABSTRACT

The "gut-skin" axis has been proved and is considered as a novel therapy for the prevention of skin aging. The antioxidant efficacy of oligomannonic acid (MAOS) make it an intriguing target for use to improve skin aging. The present study further explored whereby MAOS-mediated gut-skin axis balance prevented skin aging in mice. The data indicated the skin aging phenotypes, oxidative stress, skin mitochondrial dysfunction, and intestinal dysbiosis (especially the butyrate and HIF-1α levels decreased) in aging mice. Similarly, fecal microbiota transplantation (FMT) from aging mice rebuild the aging-like phenotypes. Further, we demonstrated MAOS-mediated colonic butyrate-HIF-1α axis homeostasis promoted the entry of butyrate into the skin, upregulated mitophagy level and ultimately improving skin aging via HDAC3/PHD/HIF-1α/mitophagy loop in skin of mice. Overall, our study offered a better insights of the effectiveness of alginate oligosaccharides (AOS), promised to become a personalized targeted therapeutic agents, on gut-skin axis disorder inducing skin aging.

1. Introduction

The skin is the largest host organ, accounting for approximately 10%–15% of the body weight and 95% of the body surface area [1]. It protects the body from external and internal environmental factors [2,3]. The skin, as a multifunctional organ, also has sensory functions and vitally affects the aesthetic appearance. However, the aging of organs including the skin begins from birth. As the outermost host tissue, the skin exhibits visible signs of aging. As a result, most people, particularly women, spend considerable money on skin care and medications that prevent or reverse skin aging. Therefore, understanding the mechanisms of skin aging can provide insights into preventing premature aging and maintaining skin health and appearance.

Alginate oligosaccharides (AOS) are natural substance produced via alginate degradation. They have high solubility and multiple bioactivities, such as immunomodulatory, anti-inflammatory, antioxidant, anti-infectious, and antitumor influences [4]. Chemically, alginate is a linear acidic polysaccharide consisting of two C5 epimers, β-D-mannuronic acid (M) and α-L-guluronic acid (G), which are uniformly or unevenly linked by 1→4 glycosidic bonds. It has an alginate structure consisting of three separate blocks: poly M, poly G, and poly MG [5]. The treatment of alginate with poly M-, poly G-, and poly MG-particular lyases yields three categories of AOS: mannuronate oligosaccharides (MAOS), guluronate oligosaccharides (GAOS), and heterogeneous mannuronate/guluronate oligosaccharides (HAOS), respectively [6]. The AOS used in research and production is usually a mixture of MAOS, GAOS, and HAOS, with HAOS being the most prevalent. Research has suggested that AOS regulates cell proliferation, differentiation, and collagen regeneration in human skin fibroblasts *in vitro* [7], implying that it may improve skin aging. Moreover, a recent study indicated that the physiological capabilities of AOS are highly rely on their structure, such as the mannuronate/guluronate (M/G) ratio, degree of polymerization residue, and spatial conformation [6]. Therefore, understanding the conformation and function of HAOS, MAOS, and GAOS is vital for their nutritional and therapeutic use in diseases such as skin aging.

The recent "gut-skin" provides new insights into the relevance between the intestinal microbiota and skin [8]. Abnormal regulation of intestinal microbes results in various inflammatory skin disorders such as atopic dermatitis, psoriasis. Increasing data reveal the presence of a gut-skin axis, where imbalances in the intestinal microbiota can cause inflammatory skin diseases [9]; however, direct intervention with prebiotics or probiotics cannot endogenously stimulate alterations in the composition of gut microbiota and therefore have a

* Corresponding author.
E-mail address: fazhengren1962@163.com (F. Ren).

https://doi.org/10.1016/j.jpha.2023.12.001

lasting and stable effect. A study showed that AOS structures differentially affect dextran sulfate sodium-caused colitis in mice via modulating the gut microbiome, indicating that AOS-mediated homeostasis of the intestinal microbiota improves host health [10]. However, the modulation control of the gut microbiome-mediated gut-skin axis by AOS requires further exploration.

Therefore, the research aimed to investigate the restorative effect of different structures of AOS on skin aging in mice, the critical role of homeostasis of the intestinal microbiota in specific AOS-mediated gut-skin axis coordination in restoring skin aging, and the potential mechanisms by which specific AOS-mediated gut homeostasis plays a regulatory role in skin aging in mice.

2. Experimental

2.1. Animals handling

Experimental practices were in accordance with the Guidelines for the Care and Use of Laboratory Animals issued by the Committee for Animal Welfare in Agricultural Research Institutions of China Agricultural University (Approval No.: CAU20170911-2 and the approval date was September 11, 2017). The stratum corneum water content (SCWC), oil content, surface pH, and skin elasticity of skin in mice were tested by the CK Skin Tester (CK-MPA10 MPA10; Courage + Khazaka electronic GmbH, Cologne, Germany).

104 male C57BL/6 mice (Vital River Laboratory Animal Technology Co., Ltd., Beijing, China) were lived on a conventional scale (temperature of 21 ± 1 °C and relative humidity of 50% ± 10%) with a 14-h light/10-h dark cycle (light started at 7 a.m.). Mice were allowed to eat and drink freely. The mice were divided into 8 groups, each with 5 experimental settings ($n = 8$).

2.1.1. Natural aging mouse model

The mice were divided into 5 groups depending on their age, including 2, 8, 12, 18, and 25 months old.

2.1.2. Different structure of AOS improved skin aging in mice

Control (CON) group (8 months); aging group (12 months, our results indicated that the 12 months old mice begin to show aging phenotype): the mice were dosed with ddH_2O (0.1 mL/mouse/day) via oral gavage as the vehicle CON for a total of 4 months from 8 months old to 12 months old; aging + HAOS, aging + MAOS, and aging + GAOS groups: HAOS, MAOS, or GAOS were administered at a content of 10 mg/kg body weight via oral gavage (0.1 mL/mouse/day) for a total of 4 months from 8 months old to 12 months old. HAOS, MAOS, and GAOS were purchased from Qingdao BZ Oligo Biotech Co., Ltd. (MAOS5K, MAPM6-8K, and MAPG3-6K; Qingdao, China). AOS (HAOS, MAOS, and GAOS) dosing solution freshly prepared daily with ddH2O. When we dilute AOS with ddH2O, 0.2 mg of AOS is dissolved per 1 mL of ddH2O, so the final diluted concentration of AOS is 0.2 mg/mL. The molecular weights of HAOS, MAOS, and GAOS were 1.93, 6.44, and 5.5 kDa, M/G ratios were approximately 2.67, 12.56, and 0.2, and purities were 93.6%, 80%, and 91.2%, respectively.

2.1.3. MAOS improved D-galactose-caused skin aging in mice

CON group (2 months); D-galactose group: D-galactose were administered at a concentration of 125 mg/kg/day via s.c injection for a total of 8 weeks; D-galactose + MAOS group: MAOS were administered at a concentration of 10 mg/kg body weight via oral gavage (0.1 mL/mouse/day) for a total of 8 weeks.

2.1.4. Fecal microbiota transplantation (FMT) experiment

Feces from mice in the CON, aging, and aging + MAOS groups were collected and set in Eppendorf tubes containing 500 mL of freezing solution (sterile saline containing 12.5% glycerol) and homogenized. The suspended particles are then stored at −80 °C. For FMT, 2 months old mice were randomly divided equally into 3 groups: F-CON (FMT from the CON group after antibiotic treatment), F-aging (FMT from the aging group after antibiotic treatment), and F-aging + MAOS (FMT from the aging + MAOS group after antibiotic treatment). For substantial depletion of the gut microbiome, the mice (F-CON, F-aging, and F-aging + MAOS) were treated with drinking water including 1 g/kg ampicillin (Santa Cruz Biotechnology, Santa Cruz, CA, USA), 100 mg/kg gentamicin (Sigma-Aldrich, St. Louis, MO, USA), 0.5 g/kg neomycin (Sigma-Aldrich), 0.5 g/kg vancomycin (Hexal, Holzkirchen, Germany), and 10 mg/kg erythromycin (Sigma-Aldrich) for 10 days. Antibiotic mix was administered by oral gavage. FMT was performed by oral administration of a fecal suspension (final volume of 0.1 mL). After 10 consecutive days of antibiotic treatment, FMT was performed daily at 7:30 a.m. for two consecutive months.

2.1.5. Methylene cyclopropyl acetic acid (MCPA) counteracts the improving effect of MAOS in mice

MCPA irreversibly suppress short-chain fatty acids (SCFA) acyl-CoA dehydrogenases, especially butyryl-CoA dehydrogenase, thereby blocking the β-oxidation of butyrate [11]. MCPA has been proved to irreversibly suppress the butyrate metabolism and decrease acetyl-CoA content by 70%–90% in rat hepatocytes [12]. The mice of CON, aging, and aging + MAOS groups were treated as in Section 2.1.2; aging + MAOS + MCPA (AMM) group: a plastic gavage tube (FTP-20-38-50, Instech, Beijing, China) was inserted 1 cm into the rectum of 8 months old mice without surgical lubricant, and 0.2 mg/mL MAOS and 10 mM MCPA were added to the drinking water and administered once a day at 7:00 a.m. for four months.

2.2. Separation of the epidermis from the dermis

After filtering the subcutaneous adipose tissue, the skin tissue was rinsed with saline, phosphate-buffered saline (PBS), and PBS containing 1% streptomycin and penicillin for three times, 5 min for each time, sequentially. Then, the skin was cut into small pieces of 0.2 cm × 0.2 cm with a scalpel, and 0.25% neutral protease II was added to it (with the surface of the liquid just submerged over the dermis, and the epidermis was exposed to the surface of the liquid), and then placed in the refrigerator at 4 °C to be digested for 14–16 h. The epidermis and dermis were separated with pointed-tooth forceps. Finally, the epidermis was separated from the dermis directly with pointed toothless forceps. When performing histology (including histological staining, transmission electron microscopy (TEM; observation of the epidermal-dermal junction), and immunohistochemistry and immunofluorescence staining), we look at the entire layer of skin tissue and can clearly see the staining and localization of the different layers of skin. We used dermal cells for Western blot, enzyme-linked immunosorbent assay (ELISA), reactive oxygen species (ROS) assay kit, etc.. Previous studies and ours collectively show that structural integrity, repair, and strength within the dermal layer of the skin determine the homeostasis of the microenvironment and skin health. In addition, mitochondrial damage in overall skin has been found to be more prevalent and measurable in dermal fibroblasts, in part due to their more quiescent phenotype, which proliferates more slowly than epidermal keratinocytes [13]. Therefore, we focused our analysis on the dermal compartment.

2.3. Histological staining

Skin and colonic tissue (fixed in 4% (*V*/*V*) para-formaldehyde) were buried in paraffin for sectioning (5-μm thickness). The skin sample were embedded in hematoxylin and eosin (H&E), Masson's

trichrome staining, and Sirius red stain. Photographs of at least 60 random areas in six sections of each sample were taken with a microscope (BX51; Olympus, Tokyo, Japan) at 400× magnification. The epidermal thickness, collagen thickness, tortuosity of the dermal-epidermal junction (DEJ), and fibrosis fluorescence value were analyzed for each specimen by the "Kappa plugin" in ImageJ software.

2.4. TEM

After rinsing with PBS, specimens were embedded in 30% sucrose in PBS, then embedded in optimal cutting temperature compound (OCT) complex (Sakura Finetechnical; Sakura Finetek, Tokyo, Japan), snap-frozen in liquid nitrogen, and set in −80 °C. Frozen samples were cut into 20-μm-thick sections using a CM 1850 cryosectioner (Leica Microsystems, Wetzlar, Germany). The epidermis was oriented using a light microscope and the frozen sections were placed on Matsunami (MAS)-coated glass slides (S9441, Matsumani Glass Ind. Ltd., Osaka, Japan). Frozen sections were washed with 0.1 M phosphate buffer, postfixed with 1% osmium tetroxide in 0.1 M phosphate buffer for 2 h, and then embedded with Epon-812. Ultrathin sections were prepared and mounted on copper grids, stained with uranyl acetate and lead citrate, and then examined by TEM (H-7100, Hitachi, Tokyo, Japan). Images were used to visualize mitochondria and DEJ in the skin.

2.5. Western blotting

Skin and colon samples were promptly embedded in liquid nitrogen and placed at −80 °C for Western blotting experiments. Total protein was extracted by lysis buffer (62.5 mmol/L Tris-HCl, 2% (*V*/*V*) sodium dodecyl sulfate (SDS), and 10% (*V*/*V*) glycerol; pH 6.8). The supernatant was acquired after centrifugation at 12,000 *g* for 10 min at 4 °C. Protein concentration was detected via a bicinchoninic acid (BCA) kit (P0012; Beyotime, Shanghai, China). Electrophoresis was operated on 20 μg of protein samples using 10% SDS-polyacrylamide gel electrophoresis (PAGE). After electrotransferring the samples onto polyvinylidene difluoride membranes (Millipore, Boston, MA, USA), the membranes were suppressed with 5% skimmed milk in 1 × triple-buffered saline (TBS) containing Tween (TBST) for 2 h at room temperature, followed by incubation with monoclonal rabbit anti-mouse primary antibody (glyceraldehyde-3-phosphate dehydrogenase (GAPDH), 1:2000; Nestin, 1:1000; collagen IV, 1:2000; COL17A1, 1:1000; Laminin 311, 1:1000; Bcl2, 1:1000; BAX, 1:1000; Caspase-3, 1:1000; Mfn2, 1:500; VDAC1, 1:1000; PINK1, 1:2000; Parkin, 1:5000; HIF-1α, 1:1000; pVHL, 1:10000; PHD, 1:1000; HDAC3, 1:2000; PPARα, 1:1000; and AMPK, 1:1000; Abcam, Cambridge, UK) overnight at 4 °C. After rinsing with TBST, goat anti-rabbit IgG was ligated to horseradish peroxidase (1:5000, CW0103; CoWin Biotech Co., Ltd., Beijing, China) via the eECL Western Blotting Kit (CW0049; CoWin Biotech Co., Ltd.) using ImageJ (version 4.0.2). Data are expressed as the integral optical density (IOD) of the Data are expressed as IOD of bands and results are from three replicate assays.

2.6. Determination of ROS formation

The ROS assay kit (Sigma-Aldrich) was used according to the instructions of the manual. After making single-cell suspensions of each group of skin tissues (using fresh skin), intracellular ROS level was tested by flow cytometry and an oxidation-sensitive dichlorodihydro-fluorescein diacetate fluorescent probe. A total of 19,105 cells were counted per treatment and the experiments was repeated three times. Changes in cells were detected using a fluorescent microplate reader.

2.7. ELISA

Total antioxidant capacity (T-AOC) concentrations were tested via a competitive ELISA kit (USCN Life Science Kit Inc., Beijing, China). The tests were manipulated depend on the indications. The values were represented as mmol/g protein in skin for the T-AOC. The intra-assay coefficient of variation (CV) was 7.9%.

2.8. Mitochondrial DNA (mtDNA) detection

The relative content of mtDNA was tested by quantitative real-time polymerase chain reaction (qPCR). The mtDNA content was tested using the $2^{-\Delta\Delta^{CT}}$ method and compared to an endogenous CON (GAPDH gene). The primer sequences for quantification of mtDNA: D41, CGAAAGGACAAGAGAAATAAGG and D56, CTGTAAAG TTTTAAGTTTTATGCG. The primer sequences for quantification of GAPDH: forward, CCACCATGGAGAAGGCTGGGGC and reverse, AGTGATGGCATGGACTGTGGTC.

2.9. Adenosine triphosphate (ATP) assay

The ATP content in the skin was detected using the ATP Determination Kit (Life Technologies, Carlsbad, CA, USA), using fresh skin tissue. The experiment is rely on luciferase's absolute require for ATP in generating light. The tissue were lysed with 500 μL of radioimmune precipitation assay (RIPA) buffer (Beyotime) and were centrifuged at 10,000 *g* for 15 min. Then, 20 μL of supernatant was mixed with 100 μL of assay buffer and loaded into a white 96-well plate. The luminescence of each well was tested using a microplate reader. The ATP standard curve was established and the ATP content was expressed as nmol/mg protein.

2.10. Immunohistochemistry and immunofluorescence staining

Skin tissue and colonic segments was cut into 5-μm cryosections and incubated with the immunohistochemistry and immunofluorescence staining. Skin tissue and colonic segments was cut into 5-μm cryosections and incubated with the immunohistochemistry and immunofluorescence staining and embedded in the following primary antibodies: HDAC3 (ab32369, 1:100; Abcam), PHD (ab173304, 1:100; Abcam), AMPK (ab32047, 1:100; Abcam), PPARα (ab227074, 1:100; Abcam), and ZO-1 (ab221547, 1:100; Abcam) for skin tissue and colon segment. More details are shown in the Supplementary data.

2.11. Intestinal microbiota sequencing

16S ribosomal RNA (rRNA) high-throughput sequencing of colonic microbiota analysis was accomplished by Shanghai Majorbio Bio-pharm Technology Co., Ltd. (Shanghai, China). We first to collect gut microbiome genomic DNA to be consistent with the manufacturer's operations by a QIAamp DNA Stool Mini Kit (Qiagen, Hilden, German). DNA fragment were PCR amplified via bar-coded primers flanking the region of V3−V4 in the 16S rRNA gene. More details are shown in the Supplementary data.

2.12. Intestinal microbiota metabolites profiling

Colonic microbiota metabolits analysis was accomplished by Shanghai Majorbio Bio-pharm Technology Co., Ltd.. We performed liquid chromatography-mass spectrometry (LC-MS) operations on a quadrupole time-of-flight (Q-TOF) 6510 mass spectrometer (Agilent Technologies, Santa Clara, CA, USA) using an electrospray ionization (ESI) source. The mass spectrometer was connected to an

Agilent 1200 high performance liquid chromatography (HPLC) system. The Q-TOF was calibrated daily using standard tuning solutions provided by Agilent Technologies. Typical mass accuracy of Q-TOF is less than 10 ppm. Due to the high number of metabolites detected, metabolites were analyzed in forward mode only in the range of m/z 80–1000 using a C_{18} reversed-phase column (Waters Corporation, Milford, MA, USA). MS/MS was generated on Q-TOF to confirm the characterization of perturbed metabolites. The metabolomics data were submitted to the XCMS Online server (https://xcmsonline.scripps.edu/).

2.13. Transcriptome sequencing analysis in skin

RNA was obtained from skin tissue using TRIzol® Reagent (Ambion; Life Technologies) and treated with DNase I (Invitrogen, Carlsbad, CA, USA) according to the manufacturer's instructions. Extracted RNA was evaluated for quality and quantity by 1% agarose gel electrophoresis and NanoDrop 2000 spectrometer (Thermo Fisher Scientific Inc., Waltham, MA, USA), and the critical value of A260/A280 was greater than 1.8. Transcriptome sequencing was performed by Shanghai Mingzhi Biomedical Science & Technology Co., Ltd. (Shanghai, China) on the Illumina HiSeq 6000 genome sequencing platform, generating 2 × 150 bp paired-end reads.

2.14. Intestinal permeability to fluorescein Isothiocyanate (FITC)-dextran

At 6:00 a.m. on the day of sampling, mice were fasted for 2 h, followed by oral administration of 0.6 mg/g body weight 4 kDa FITC-dextran at a content of 80 mg/mL 1 h before euthanasia. About 1 mL of blood was harvested via retro-orbital eye bleed and centrifuged (500 *g*, 10 min) to gain serum (about 500 μL). The serum fluorescence was detected by a fluorescent spectrophotometer. The standard curve was set through FITC-dextran diluted in PBS. The FITC-dextran content in the serum was counted by the standard curve.

2.15. Butyrate extraction and analysis

Collected mouse fecal contents were stayed with −80 °C. The feces were mixed with water and centrifuged. Superior water is a mixture of sulfuric acid and water. The concentration of sulfuric acid increases over time by centrifugal force at high speed.

2.16. Statistical analysis

Data are expressed as the mean ± standard error and were analyzed using SPSS 10.0 statistical software (SPSS Inc., Chicago, IL, USA). Differences between groups were statistically analyzed using analysis of variance (ANOVA) followed by one-way ANOVA, which were used to determine the significance of differences among groups ($^{*}P < 0.05$, $^{\#}P < 0.01$, and $^{\&}P > 0.05$).

3. Results and discussion

3.1. Alterations in skin physical indicators and skin structure with age in mice

The skin is the largest host organ and acts as a barrier against many kinds of damage. It constitutes the basic defense against various environmental toxins, thus protecting the internal organs. Its strategic location is regarded as a key barrier linking the external and internal environments, and an important tool for maintaining balance [14]. However, the skin exhibits signs of regression, leading to an appearance of aging and several pathological processes [15]. Therefore, we first examined the changes in skin physiological indicators and skin structure in different age and different tissues, including face, back, abdomen and ears of 2-, 8-, 12-, 18-, and 25 months old mice (Fig. 1A). Fig. 1B exhibited the appearance of the mouse in different age. Further, we observed the physiological indicators including moisture, elasticity, oil, and pH changed after 8 months (Figs. 1C–F and S1). Among them, the decrease in skin moisture and skin elasticity of facial skin is the most obvious, indicating a significant decrease in skin moisture and elasticity with age. Therefore, our next observations on the skin structure of mice at different months of age mainly focused on the facial skin of mice.

The H&E staining (Figs. 1G and H) and masson's trichrome staining (Figs. 1I and J) results showed the structure of the different layers of the skin, including epidermis, dermis, and subcutaneous tissue. Statistically, the epidermal thickness and collagen thickness gradually reduced with age (Figs. 1H and J). Moreover, polarized light microscopy identified progressive fibrosis in the dermis (Fig. 1K). The data showed that the fibrosis area significantly increased after 12 months old (Fig. 1L). Further observation of the epidermal-dermal junction changes in the skin of mice at different months of age under TEM, and the data suggested the tortuosity of DEJ gradually flattened with age (Figs. 1M and N), indicating that the area of nutrient transport from the dermis to the epidermis is gradually decreasing with age.

In summary, our results showed that the skin moisture and skin elasticity of mice progressively decreased with age, and were accompanied by changes in skin structure, as evidenced by the decrease in epidermal thickness, dermal thickness and curvature of the DEJ, and the increase in skin fibrosis.

3.2. Effect of different structures of AOS on skin structure changes in aging mice

To investigate whether different structures of AOS, including HAOS, MAOS, and GAOS, could exert a salutary effect on skin aging, we set up a natural aging mouse model with or without HAOS, MAOS, or GAOS supplementation. Our results suggested that HAOS, MAOS, or GAOS supplementation significantly upregulated the skin stratum corneum water content (SCWS) (Fig. 2A), skin elasticity (Fig. 2B), epidermal thickness (Figs. 2C and D), collagen thickness (Figs. 2E and F), reduced fibrotic area (Figs. 2G and H), and increased the DEJ tortuosity (Figs. 2I and J) in aging mice to varying degrees. Among them, MAOS has a more outstanding improvement effect.

Specifically, DEJ is composed of four main proteins, including Nestin, collagen IV, COL17A1, and Laminin 311. Our results suggested that the concentrations of these four proteins (Figs. 2K–N) decrease progressively in aging mice versus CON group. Moreover, the supplementation of HAOS, MAOS, and GAOS all differentially upregulated the expression of these four proteins, with MAOS showing a more pronounced increase. Similarity, a homogeneous suspension of AOS has proved to stimulate the proliferation of normal human skin fibroblasts [16] via stimulating keratinocyte proliferation in the presence of epidermal growth factor (EGF) [17]. The results showed that the different structures of AOS could improve skin aging to different degrees, and the improvement effect of MAOS was due to the other two structures of AOS.

3.3. Effect of different structures of AOS on skin mitochondrial dysfunction in aging mice

Skin function is maintained via cooperation between the epidermis, dermis, and DEJ; it is a high-turnover process that depends on ATP as an energy source. ATP is mainly derived from oxidative phosphorylation in the mitochondria, which are known

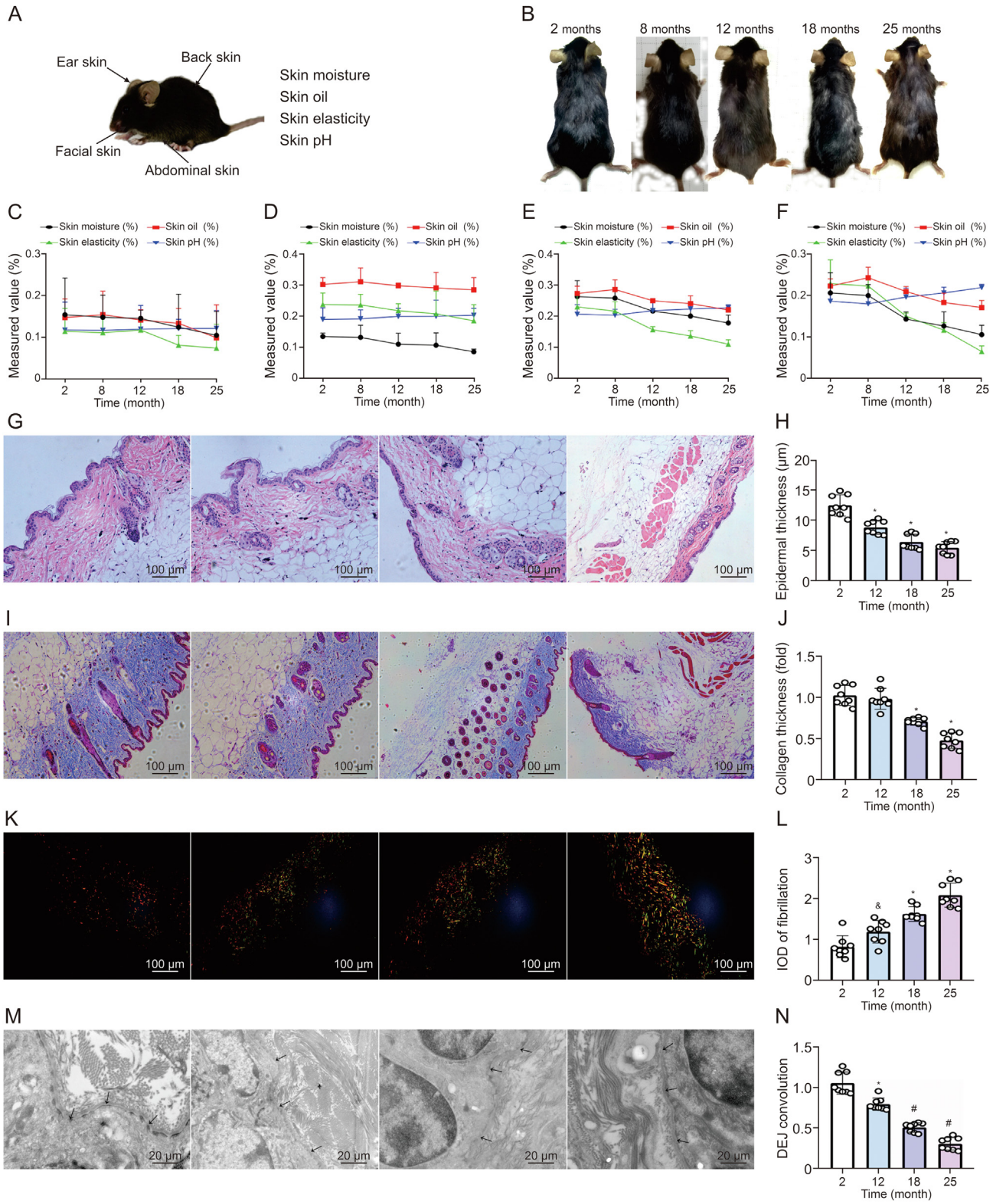

Fig. 1. Changes in skin physiological indicators and skin structure with age in mice. (A) Source of skin collected and skin indicators tested. (B) Back pictures of mice in different months. (C–F) The value of skin physiological indicators, including skin moisture, skin oil, skin elasticity and skin pH in ear (C), abdomen (D), back (E), and face (F). (G, H) Hematoxylin and eosin (H&E) staining of skin structure (G) and epidermal thickness (H). (I, J) Masson's trichrome staining of skin collagen (I) and collagen thickness (J). (K, L) Sirius red staining (K) and integral optical density (IOD) of fibrillation (L). (M, N) Transmission electron microscopy (TEM) observation of dermal-epidermal junction (DEJ) (M) and DEJ convolution (N) measured in skin of 2-, 12-, 18-, and 25 months old mice, respectively. Values are presented as the means ± standard deviation. Differences were assessed by analysis of variance (ANOVA) and denoted as follows: $^{*}P < 0.05$, $^{\#}P < 0.01$, and $^{\&}P > 0.05$, compared to 2 months.

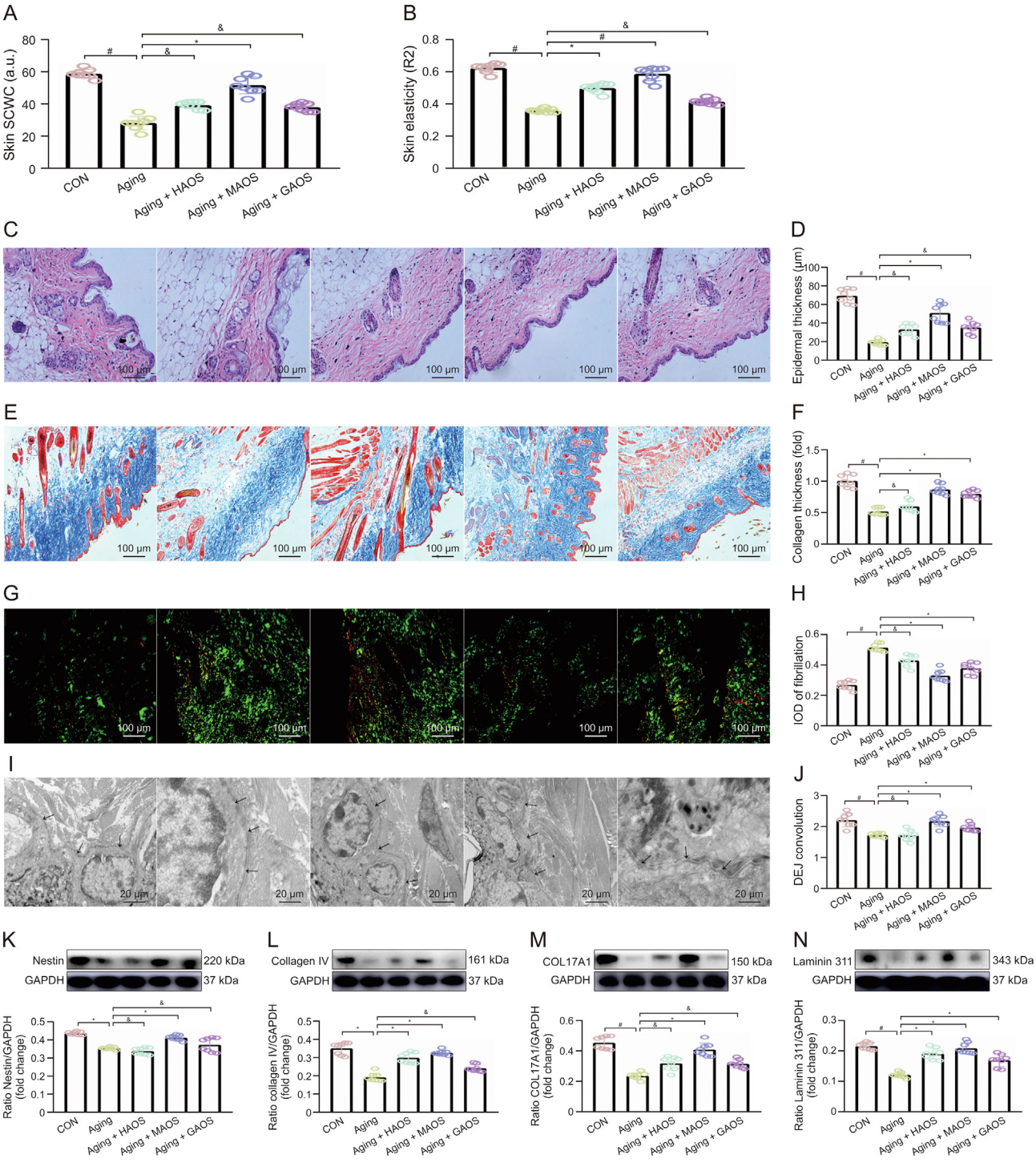

Fig. 2. Effect of different structures of alginate oligosaccharides (AOS) on skin structure changes in aging mice. (A, B) Skin stratum corneum water content (SCWC) (A) and skin elasticity (B) were measured in skin of control (CON), aging, aging + heterogeneous mannuronate/guluronate oligosaccharides (HAOS), aging + mannuronate oligosaccharides (MAOS), and aging + guluronate oligosaccharides (GAOS) groups, respectively. (C, D) Hematoxylin and eosin (H&E) staining of skin structure (C) and epidermal thickness (D). (E, F) Masson's trichrome staining of skin collagen (E) and collagen thickness (F). (G, H) Sirius red staining of skin fibrosis (G) and integral optical density (IOD) of fibrillation (H). (I, J) Transmission electron microscopy (TEM) observation of dermal-epidermal junction (DEJ) junction in skin of different groups (I) and DEJ convolution measured in skin of CON, aging, aging + HAOS, aging + MAOS, and aging + GAOS groups, respectively (J). (K–N) Relative protein levels of Nestin (K), collagen IV (L), COL17A1 (M), and Laminin 311 (N) protein productions were normalized to glyceraldehyde-3-phosphate dehydrogenase (GAPDH) using Western bloting. CON: 8 months; aging: 12 months; and aging + AOS (HAOS, MAOS, and GAOS): 12 months; the concentration of AOS (HAOS, MAOS, and GAOS): 10 mg/kg. Values are presented as the means ± standard deviation. Differences were assessed by analysis of variance (ANOVA): $^{*}P < 0.05$, $^{\#}P < 0.01$, and $^{\&}P > 0.05$, compared to aging group.

bioenergy centers in eukaryotic cells [18]. However, the skin aging is accompanied by the accumulation of oxidative products and oxidative stress-mediated mitochondrial dysfunction in most cells. Excessive ROS production in mitochondria causes mitochondrial dysfunction, which further damages these organelles [19]. Further, we examined antioxidant markers, including ROS and T-AOC (Figs. 3A and B), and apoptotic markers, including Bcl2, Bax, and Caspase-3 (Fig. 3C–E), in the skin of different groups. Our results indicated

that the production of mitochondrial ROS content and concentration of Bax and Caspase-3 proteins increased significantly (Figs. 3A, D, and E), while the levels of T-AOC and Bcl2 protein decreased obviously (Figs. 3B and C) in aging mice versus CON mice. Further, in the skin of CON mice, mitochondria are short rod-shaped and evenly distributed (Fig. 3F). While with age, mitochondria are irregular thin strips or round, and the number is significantly increased. Statistically, the mtDNA and ATP contents obviously reduced (Figs. 3G and H) in aging mice compared with CON mice. Structurally, mitochondrial functional stabilization is tightly regulated by mitochondrial dynamics including fission, fusion, and mitophagy [20]. As an adaptive response to stress, mitochondrial phagocytosis plays an important role in cellular homeostasis via eliminating dysfunctional mitochondria and reducing mitochondrial mass [21]. Moreover, compared to those in CON mice, the concentration of Mfn2, VDAC1, Parkin, and PINK1 proteins decreased significantly in aging mice (Figs. 3I–L), suggesting that the mitophagy level gradually decreases with age, manifesting as

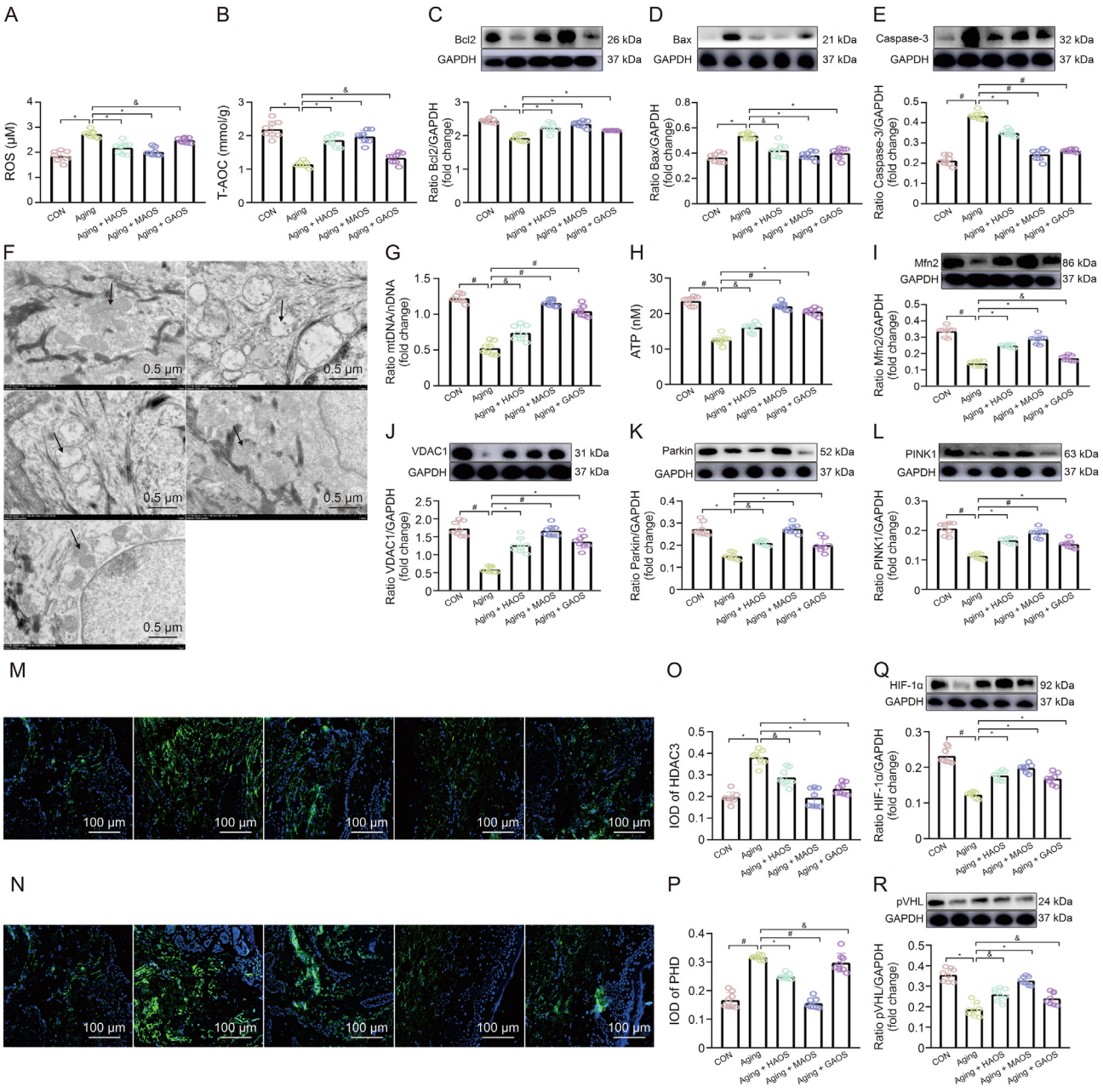

Fig. 3. Effect of different structures of alginate oligosaccharides (AOS) on skin mitochondrial dysfunction in aging mice. (A, B) Reactive oxygen species (ROS) (A) and total antioxidant capacity (T-AOC) (B) levels. (C–E) Relative protein levels of Bcl2 (C), Bax (D), and Caspase-3 (E) protein productions. (F) Transmission electron microscopy (TEM) observations of mitochondria. (G, H) mitochondrial DNA (mtDNA)/nuclear DNA (nDNA) (G) and adenosine triphosphate (ATP) (H) contents. (I–L) Mfn2 (I), VDAC1 (J), Parkin (K), and PINK1 (L) protein productions were normalized to glyceraldehyde-3-phosphate dehydrogenase (GAPDH) using Western bloting. (M, N) Immunofluorescent staining in HDAC3 (M) and PHD (N) protein. (O–R) The integral optical density (IOD) of HDAC3 (O) and PHD (P), HIF-1α (Q) and pVHL (R) protein productions in skin of control (CON), aging, aging + heterogeneous mannuronate/guluronate oligosaccharides (HAOS), aging + mannuronate oligosaccharides (MAOS), and aging + guluronate oligosaccharides (GAOS) groups, respectively. CON: 8 months; aging: 12 months; and aging + AOS (HAOS, MAOS, and GAOS): 12 months; the concentration of AOS (HAOS, MAOS, GAOS): 10 mg/kg. Values are presented as the means ± standard deviation. Differences were assessed by analysis of variance (ANOVA) and denoted as follows: $^{*}P < 0.05$, $^{\#}P < 0.01$, and $^{\&}P > 0.05$, compared to aging group.

mitochondrial dysfunction and ultimately resulting in oxidative stress and apoptosis response. Similarity, a previous study indicated that a reduction in mitophagic activity is associated with aging and neurodegenerative disorders, emphasizing the vital role of mitochondrial quality control in maintaining longevity [22,23]. Moreover, the supplementation of different structures of AOS alleviated mitochondrial dysfunction and its induced oxidative stress and apoptotic response in aging skin, with MAOS having the most pronounced alleviating effect (Figs. 3A–L).

Further, date showed the expression levels of HDAC3 and PHD (Figs. 3M–P) proteins obviously increased, while HIF-1α and pVHL proteins contents gradually decreased with age (Figs. 3Q and R) in skin of aging mice versus CON group. However, different structure of AOS exert an improvement effect on it, and the MAOS supplementation showed a the most prominent performance.

In summary, our results illustrated that with age, mitophagy level in skin gradually decreases, accompanied by the accumulation of injury mitochondria in the cell, further inducing mitochondrial apoptosis occurrence and ATP production decrease, ultimately resulting in cell death and insufficient energy supply-mediated fibrosis. However, MAOS supplementation has played a very significant role in improving skin aging (Fig. S2).

3.4. Effect of MAOS on skin aging in D-galactose-treated mice

To further survey the ameliorative influence of MAOS in skin aging, we established a D-galactose-induced skin aging model with or without MAOS supplementation. Our results suggested that MAOS supplementation significantly upregulated epidermal thickness, collagen thickness, and DEJ tortuosity, and reduces fibrotic area in aging mice (Figs. 4A–H). Moreover, there was a downregulation in the expression levels of Nestin, collagen IV, COL17A1, and Laminin 311 proteins (Figs. 4I–L) in D-galactose-treated mice compared with CON mice, while the MAOS

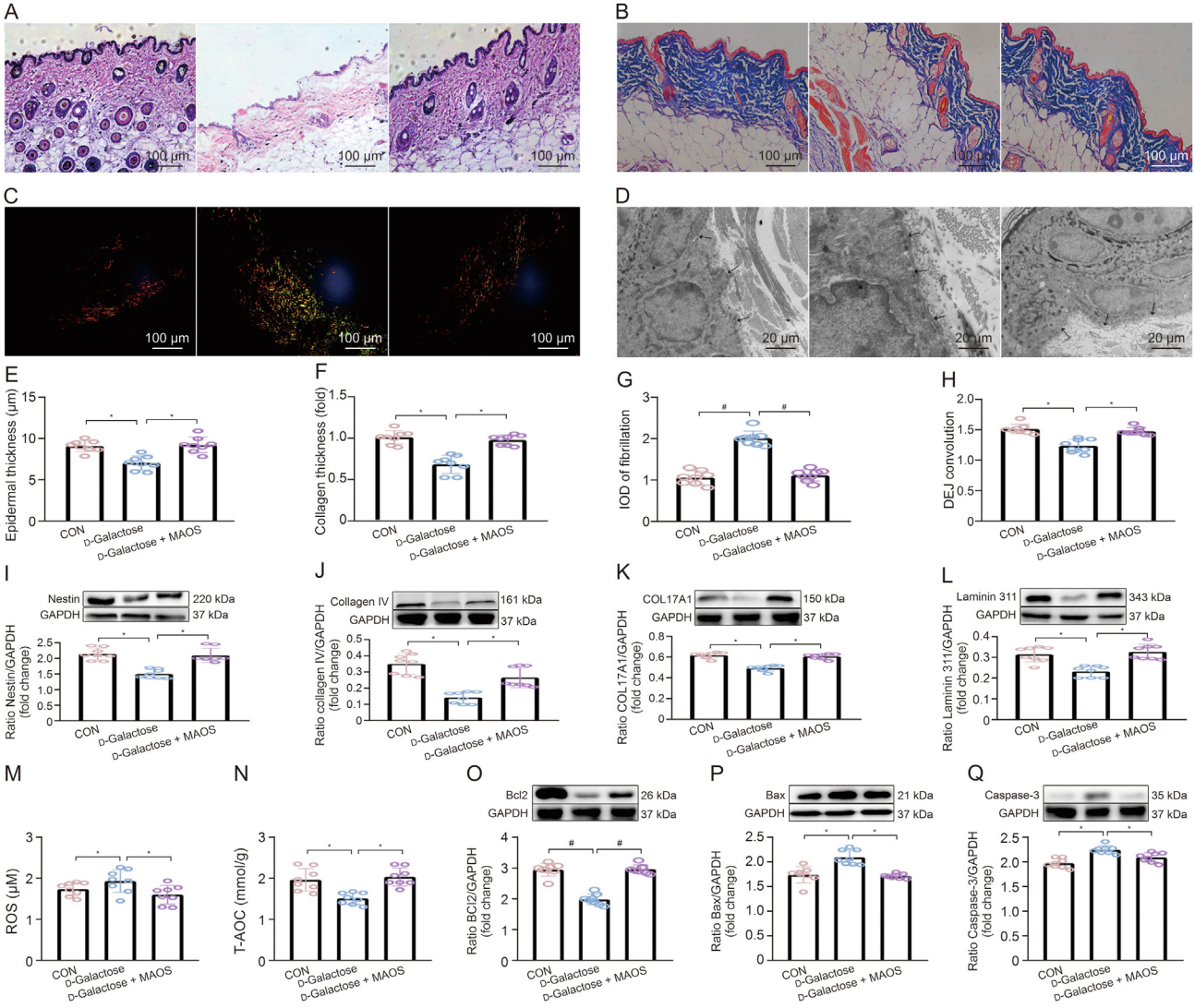

Fig. 4. Effect of mannuronate oligosaccharides (MAOS) on skin aging in D-galactose-treated mice. (A–D) Hematoxylin and eosin (H&E) staining of skin structure (A), Masson's trichrome staining of skin collagen (B), sirius red staining of skin fibrosis (C), and transmission electron microscopy (TEM) (D) observations of dermal-epidermal junction (DEJ) junction in back skin of control (CON), D-galactose, and D-galactose + mannuronate oligosaccharides (MAOS) groups. (E–H) Epidermal thickness (E), collagen thickness (F), fibrosis fluorescence value (G), and DEJ convolution (H) were measured in skin of CON, D-galactose, and D-galactose + MAOS groups, respectively. (I–L) Relative protein levels of Nestin (I), collagen IV (J), COL17A1 (K), and Laminin 311 (L) protein productions. (M, N) Reactive oxygen species (ROS) (M) and total antioxidant capacity (T-AOC) (N) levels. (O–Q) Bcl2 (O), Bax (P) and Caspase-3 (Q) protein productions were normalized to glyceraldehyde-3-phosphate dehydrogenase (GAPDH) using Western bloting and enzyme-linked immunosorbent assay (ELISA) in skin of CON, D-galactose, and D-galactose + MAOS groups, respectively. The mice in CON, D-galactose, and D-galactose + MAOS groups are 2 months old and the concentration of MAOS is 10 mg/kg. Values are presented as the means ± standard deviation. Differences were assessed by analysis of variance (ANOVA) and denoted as follows: $^{*}P < 0.05$, $^{\#}P < 0.01$, and $^{\&}P > 0.05$, compared to D-Glactose group. IOD: integral optical density.

supplementation played a vital role on it. Further, we examined antioxidant markers, including ROS and T-AOC (Figs. 4M and N), and apoptotic markers, including Bcl2, Bax, and Caspase-3 (Figs. 4O–Q), in the skin of different groups. We found there was an oxidative stress in the skin of D-galactose-treated mice, accompanied by the upregulation in the ROS level, Bax and Caspase-3 proteins (Figs. 4M, P, and Q), and the decrease in the levels of T-AOC and Bcl2 proteins (Figs. 4N and O). However, MAOS supplementation significantly suppressed the occurrence of oxidative stress in aging mice.

Overall, these results indicated the ROS accumulate in mouse skin with age, triggering an apoptotic response that leads to structural skin damage, while MAOS supplementation effectively reverses this process and improves skin aging.

3.5. Alterations in gut microbiota and its metabolites composition with age in mice

Changes in the ingredient of the intestinal microbiota and its metabolites could cause pathological changes in multiple diseases,

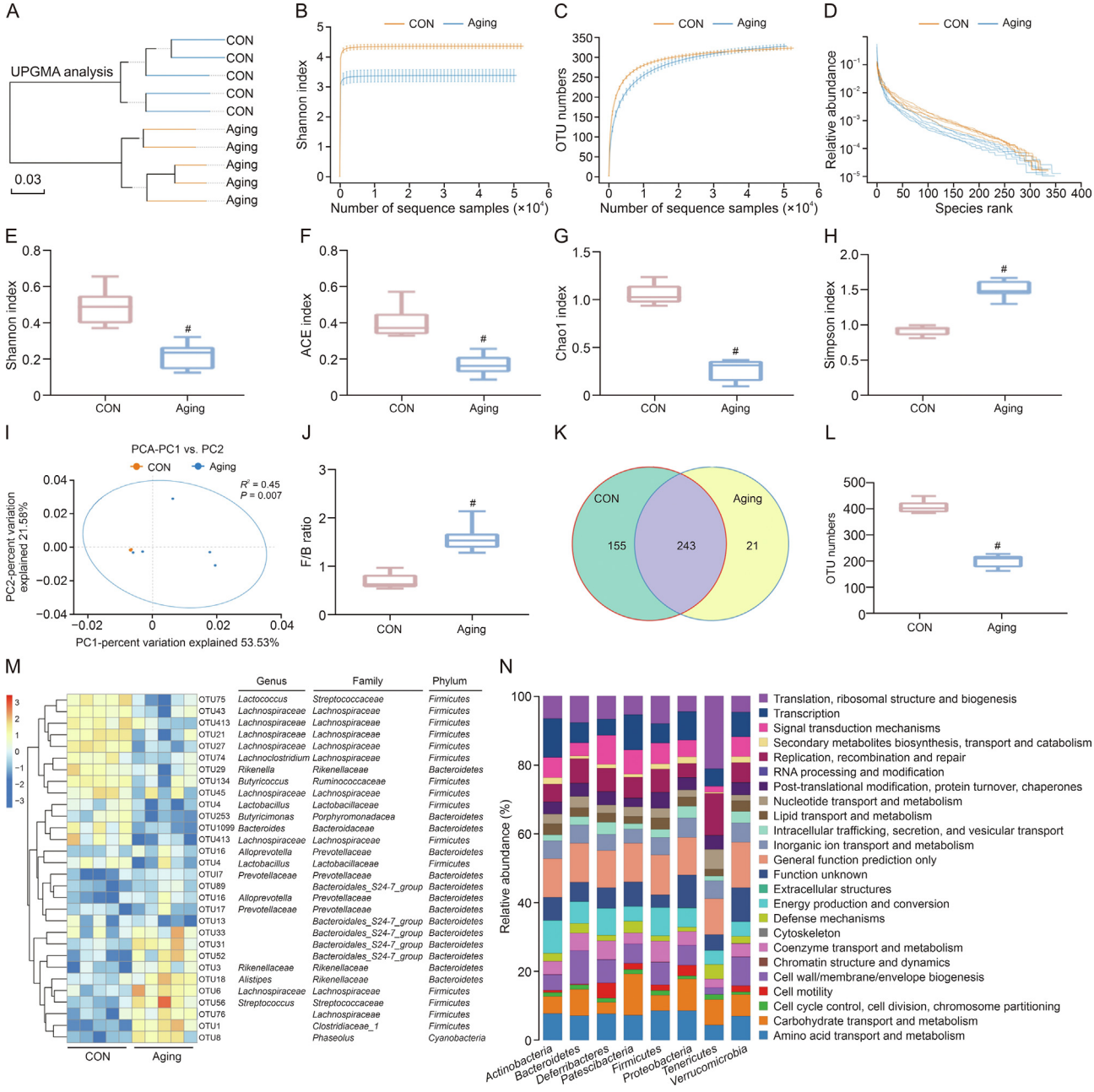

Fig. 5. Changes in intestinal microbiota composition with age in mice. (A) The unweighted pair-group method with arithmetic means (UPGMA) analysis. (B–D) The α diversity includes diversity and richness: the muti samples Shannon curves (B), multi-samples rarefaction curves (C), and species rank (D); (E–H) Shannon index (E), abundance-based coverage estimator (ACE) index (F), Chao1 index (G), and Simpson index (H) between control (CON) and aging groups. (I) The β diversity: principal component analysis (PCA) score plot based on the Bray-Curtis score plot and the operational taxonomic units (OTU) in the feces. (J) *Firmicutes*/*Bacteroidetes* (F/B) ratio of intestinal microbiota. (K, L) Distribution of the number of OTUs in the CON vs. Aging group: Venn diagram of OTUs (K) and OTU number (L); (M) Heatmap of the redundancy analysis (RDA)-identified key OTUs and linear discriminant analysis (LDA) effect size (LefSe) identifying the most differentially abundant taxons in intestinal microbiota in response to aging. (N) Significantly varying intestinal microbiota and their corresponding functions. CON: 8 months and aging: 12 months. Values are presented as the means ± standard deviation. Differences were assessed by analysis of variance (ANOVA) and denoted as follows: $^{*}P < 0.05$, $^{\#}P < 0.01$, and $^{\&}P > 0.05$, compared to CON group. PC: principal component.

such as aging [24,25], and a disordered intestinal microbiota, a pathological status termed as gut dysbiosis, which exerts a negative influence on skin structure and function. Therefore, considering the important role of changes in gut microbiota and its metabolites composition in skin aging, we tested the gut microbiota and its metabolites composition in CON and aging mice (Fig. 5A). High-throughput sequencing data indicated these was an obvious decrease in the microbiota diversity and richness (Figs. 5B–H), reflected in the decrease in Shannon index, ACE index, and Chao1 index (Figs. 5E–G) and the increase in Simpson index (Fig. 5H), while the intestinal microbiota dispersion and *Firmicutes*/*Bacteroidetes* (F/B) ratio increased significantly in aging group compared with CON group (Figs. 5I and J), which are important factors in structural revisions of the gut microbiota [26]. Further, there was an obvious downregulation in the operational taxonomic units (OTU) number in aging group versus CON group (Figs. 5K and L). Moreover, the heatmap analysis indicated the levels of *Alloprevotella, Prevotellaceae*, and *Rikenellaceae* obviously increased, while the contents of *Lachnospiraceae*, *Butyricicoccus*, and *Butyricimonas* obviously decreased, which were butyrate-producing bacteria, in aging group versus CON group (Fig. 5M). Several reports have described that many skin disorders are accompanied by changes in intestinal microbiota [27,28]. Further, Kyoto Encyclopedia of Genes and Genomes (KEGG) results showed that these altered intestinal microbiota were mainly associated with the pathways of amino acid transport and metabolism, carbohydrate transport and metabolism, cell motility, cell wall/membrane/envelope biogenesis, etc. (Fig. 5N).

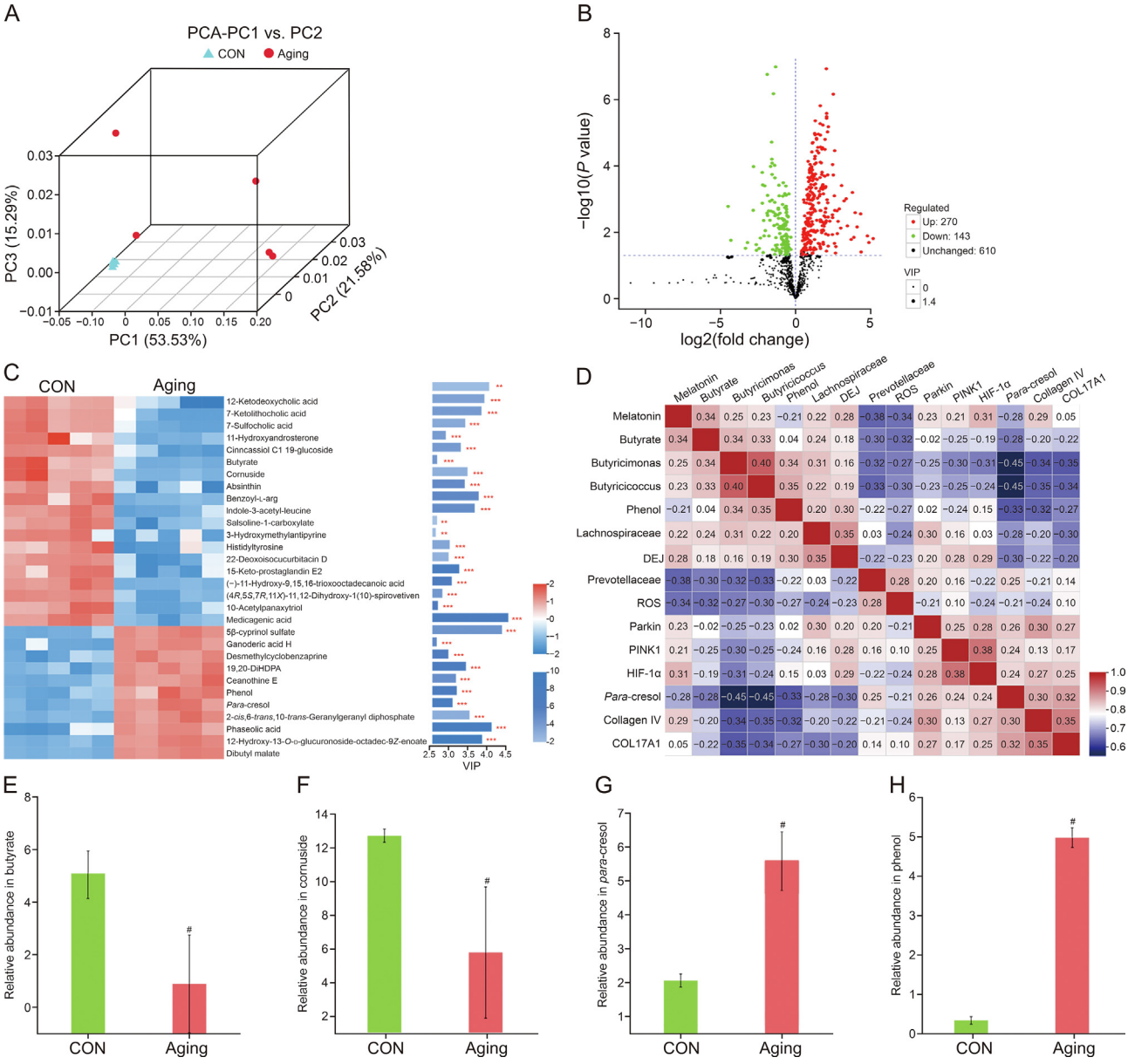

Fig. 6. Changes in intestinal microbiota metabolites composition with age in mice. (A) The β-diversity of principal component analysis (PCA). (B) Volcano plot based on the differential metabolite screening, compared with the control (CON) and aging groups. (C) Heatmap showing the relative abundance of the key identified 30 metabolites that were significantly altered in aging mice. (D) Correlation of significantly altered intestinal microbiota and its metabolites with skin function. (E–H) The relative abundance of butyrate (E), cornuside (F), para-cresol (G), and phenol (H) in CON and aging groups. CON: 8 months and aging: 12 months. Values are presented as the means ± standard deviation. Differences were assessed by analysis of variance (ANOVA) and denoted as follows: $^{*}P < 0.05$, $^{\#}P < 0.01$, and $^{\&}P > 0.05$, compared to CON group. PC: principal component; VIP: variable importance in the projection; DiHDPA: docosahexaenoic acid; DEJ: dermal-epidermal junction; ROS: reactive oxygen species.

Further, we explored the disproportionality in microbiota metabolites of aging group. β-diversity analysis indicated an obvious upregulation in the dispersion of intestinal microbiota metabolite, showing a downregulation in the homogeneity of intestinal microbiota metabolite (Fig. 6A) in aging group compared with CON group. Further, compared with the CON group, 270 metabolites were increased and 143 metabolites were decreased in aging group (Fig. 6B). Further, we selected the 30 most altered microbiota metabolites among the two groups (Fig. 6C). We correlated the changed intestinal microbiota and its metabolites with altered skin metrics and showed that a decrease in butyrate was significantly and positively correlated with a decrease in DEJ curvature, collagen IV, COL17A1, HIF-1α, and mitophagy levels (Fig. 6D). Moreover, the results demonstrated the contents of butyrate, cornuside, absinthin, and indole-3-acetyl-leucine, etc. significantly decreased, while the contents of ganoderic acid H, desmethylcyclobenzaprine, phenol, and para-cresol, etc. increased obviously in aging group versus CON group. Specifically, the levels of butyrate and cornuside obviously decreased, while the contents of para-cresol and phenol obviously upregulated in aging group compared with CON group (Figs. 6E–H). Studies have shown that phenol and p-cresol can damage the epidermal barrier integrity via decreasing keratin 10 expression in keratinocytes [29,30]. Moreover, age-related dysbiosis, including butyrate level reduction, further exacerbates the progression of aging, inflammation, and weakness, negatively affecting systemic health and longevity [31].

In summary, with aging, there was an intestinal microbiota and its metabolites disorder, which is closely associated with skin aging.

3.6. Changes in skin transcriptome analysis with age in mice

To further investigate the intrinsic mechanisms of skin aging, we carried out transcriptome analysis on two groups of skin from CON and senescent mice. The β-diversity analysis showed that the

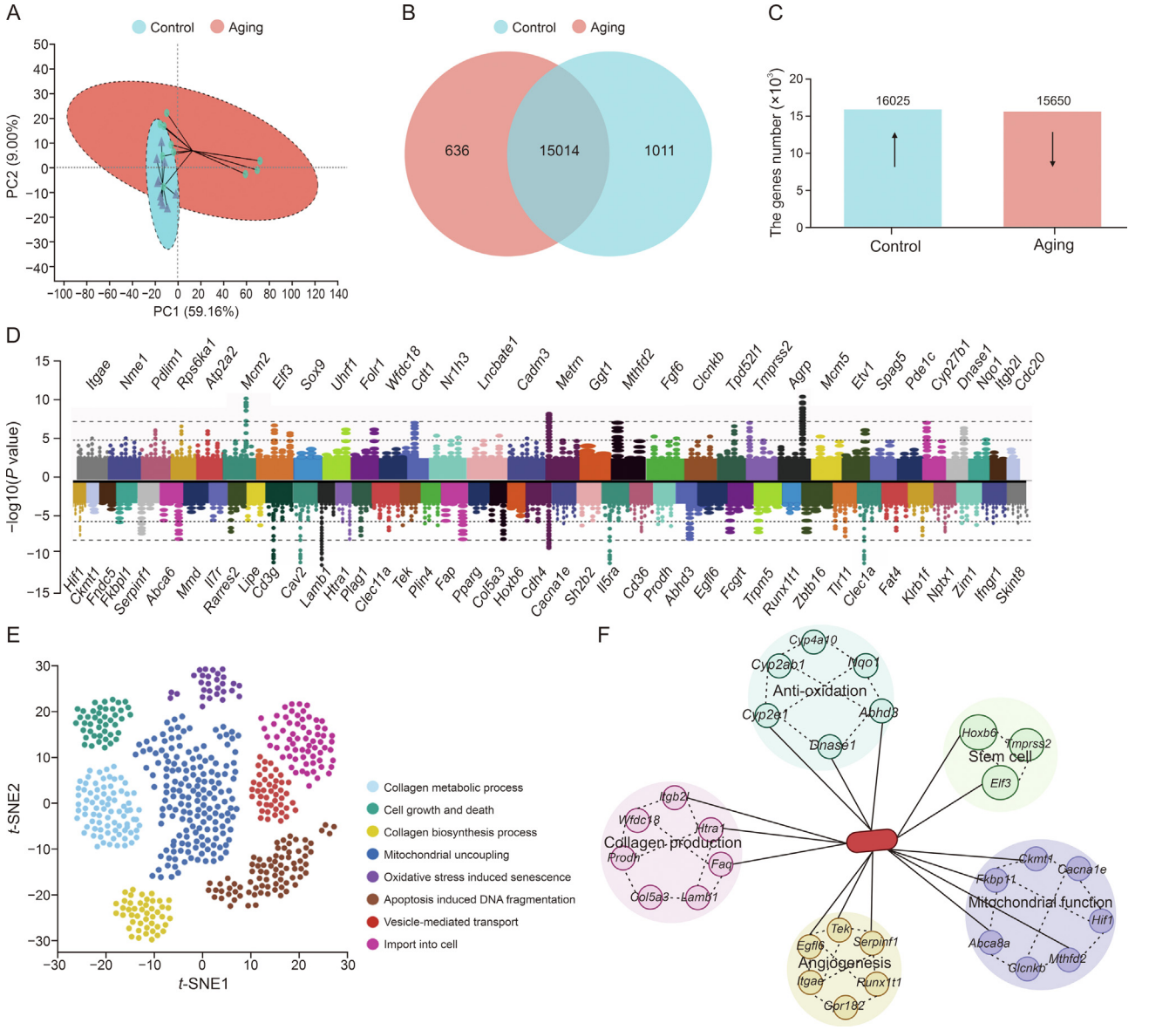

Fig. 7. Changes in skin transcriptome analysis with age in mice. (A) The β-diversity of principal component analysis (PCA). (B, C) Venn diagram based on the differential transcribed genes screening, compared with the control (CON) and aging groups (B) and the upregulated (↑) and downregulated (↓) genes expressed in the CON vs. aging groups ($P < 0.001$) (C). (D) Horizontal bars represent the log2(fold change) comparison (upregulated genes in aging group: log2(fold change) > 0 and downregulated genes in aging mice: log2(fold change) < 0). (E, F) Genes involved in different facets of skin function in CON and aging groups (E) and genes enriched in different functions (F). CON: 8 months and aging: 12 months. Values are presented as the means ± standard deviation. PC: principal component; *t*-SNE: *t*-distributed stochastic neighbour embedding.

transcriptome data exhibited significant clustering, indicating a marked upregulation in the dispersion of the data in the senescent group compared to the CON group (Fig. 7A). Specifically, there were 15,014 same genes in these two groups (Figs. 7B and C). We then enriched and drafted the 74 most obviously altered genes into a heatmap (Fig. 7D). Specifically, there were 32 genes significantly upregulated, including Itgb21, Wfdc18, Clcnkb, and Nqo1, and 42 genes obviously downregulated, including Hif1, Ckmt1, Fndc5, and Fkbp11. Afterwards, we further functionally analyzed the genes enriched for skin functions and uncovered that a lots of these genes are associated with collagen production and degradation, including collagen metabolic process, cell growth and death, collagen

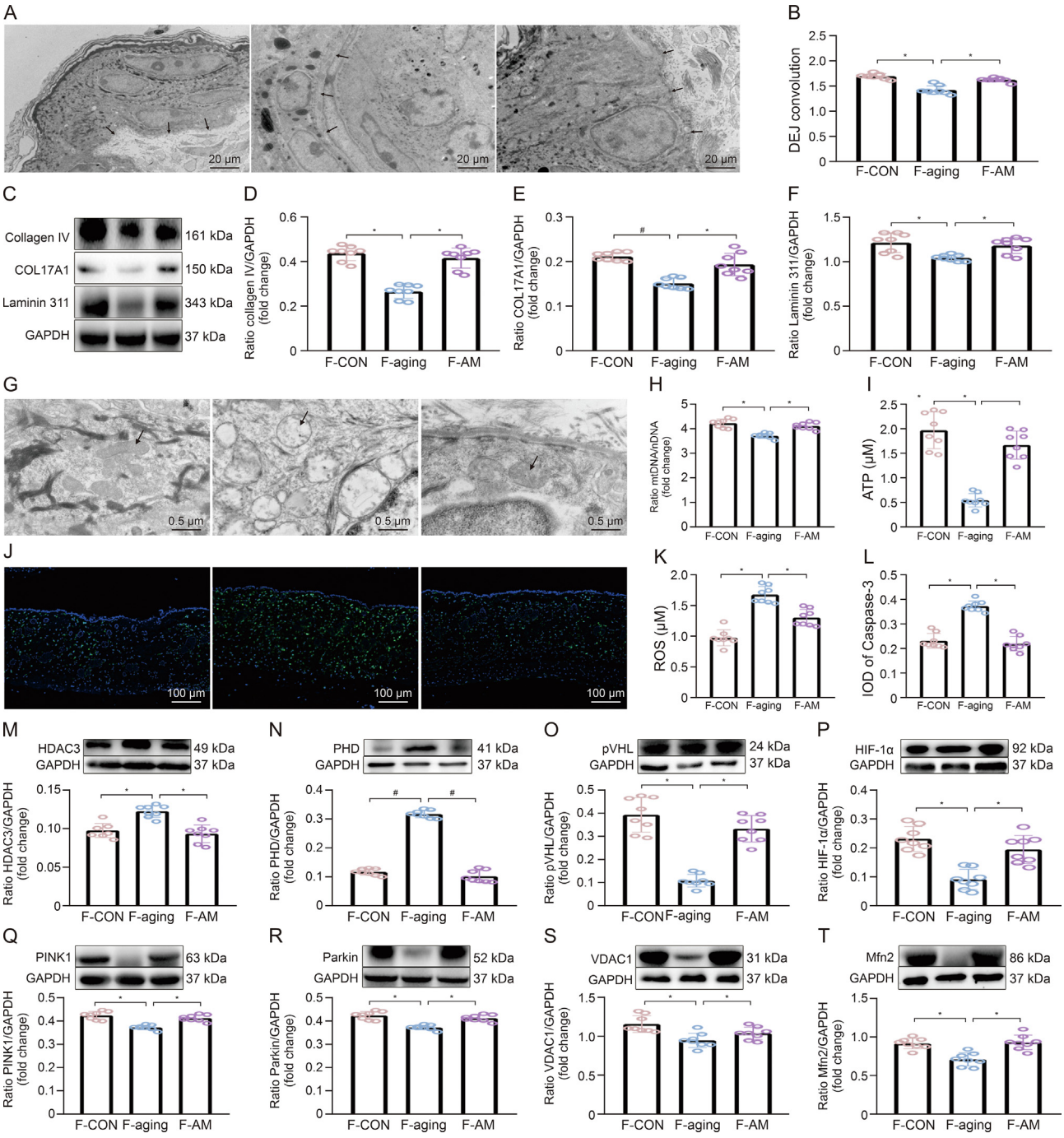

Fig. 8. Fecal microbiota transplantation (FMT) re-established the skin status similar to control (CON), aging, and aging + mannuronate oligosaccharides (MAOS) mice. (A, B) Transmission electron microscopy (TEM) observation of dermal-epidermal junction (DEJ) structure (A) and DEJ convolution (B) in back skin. (C–F) Western blot (C) and relative protein levels of collagen IV (D), COL17A1 (E), and Laminin 311 (F) protein productions normalized to glyceraldehyde-3-phosphate dehydrogenase (GAPDH). (G–K) TEM observations of mitochondria (G), mitochondrial DNA (mtDNA)/nuclear DNA (nDNA) (H), and adenosine triphosphate (ATP) (I) contents.(J) Immunofluorescence staining in Caspase-3. (K) Reactive oxygen species (ROS) were measured by enzyme-linked immunosorbent assay (ELISA) and mtDNA detection kit. (L) The integral optical density (IOD) of Caspase-3. (M–T) HDAC3 (M), PHD (N), pVHL (O), HIF-1α (P), PINK1 (Q), Parkin (R), VDAC1 (S), and Mfn2 (T) protein productions were normalized to GAPDH using Western bloting in skin of FMT from CON group (F-CON), FMT from aging group (F-aging), and FMT from aging + MAOS group (F-AM), respectively. The mice in F-CON, F-aging, and F-AM groups are 2 months old. Values are presented as the means ± standard deviation. Differences were assessed by analysis of variance (ANOVA) and denoted as follows: $^{*}P < 0.05$, $^{\#}P < 0.01$, and $^{\&}P > 0.05$, compared to F-aging group.

biosynthesis process, mitochondrial uncoupling, oxidative stress induced senescence, apoptosis induced DNA fragmentation, vesicle-mediated transport, and import into cell (Fig. 7E). Further, these genes are mainly related to five skin-associated functions, including anti-oxidative, stem cell proliferation and differentiation, mitochondrial function, collagen regeneration, and angiogenesis (Fig. 7F).

The results of skin transcriptome results are consistent with the outcomes of *in vivo* experiments that skin aging is accompanied by mitochondrial dysfunction and oxidative stress, which may also be an effective way to intervene in skin aging. Importantly, the decrease in HIF-1α can exert a vital effect in reduced mitophagy-mediated skin aging. Several previous studies have demonstrated that HIF-1α participates in mitochondrial apoptosis modulation [32]; however, its potential mechanisms remain unknown. Similarly, Lin et al. [33] demonstrated that HIF-1α deficiency decreased the mitophagy level, and thus mitophagy could be increased via upregulating HIF-1α expression, which removed damaged mitochondria, restored cellular homeostasis, and ameliorated oxidative stress.

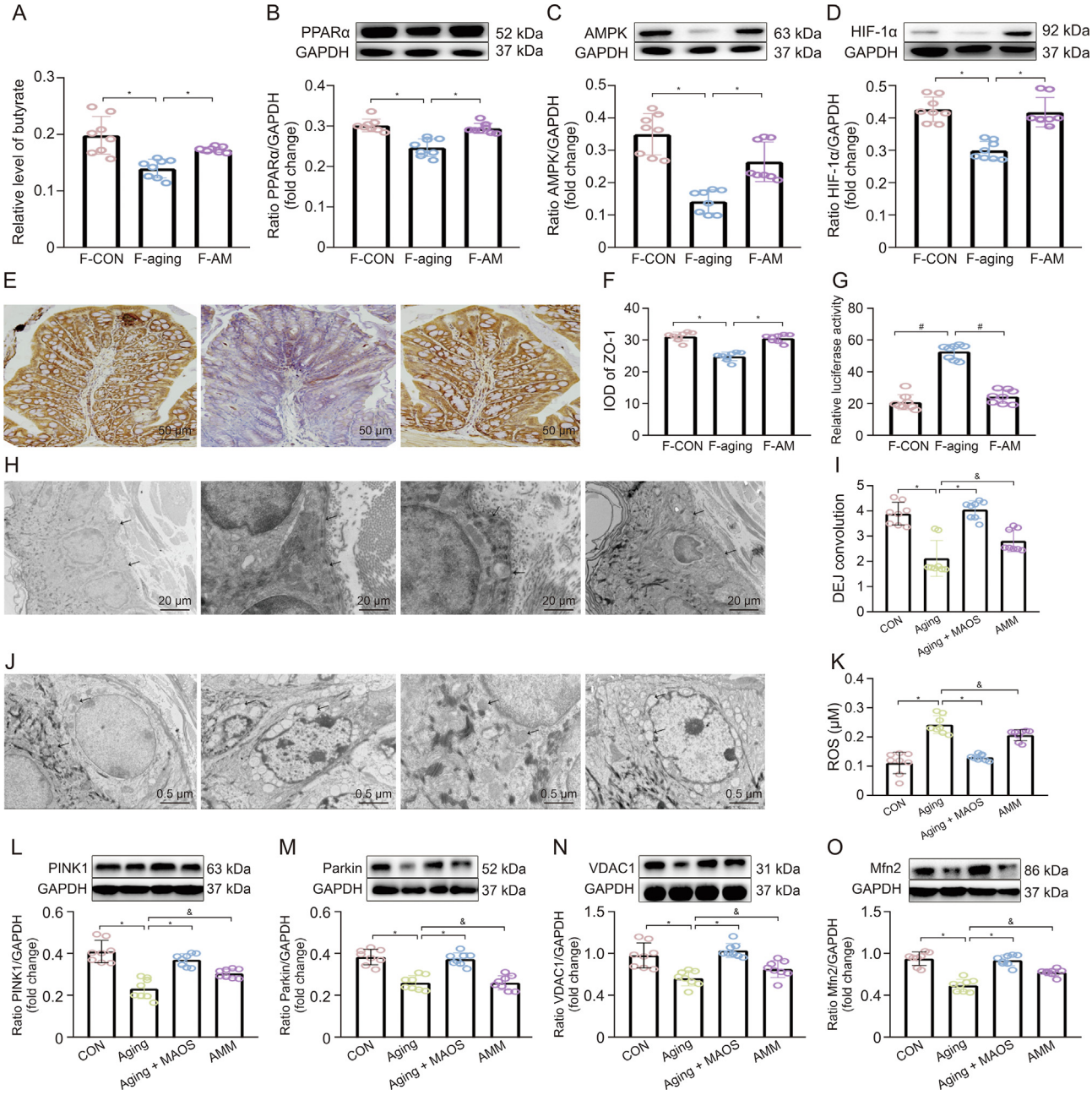

Fig. 9. 2-Methyl-4-chlorophenoxyacetic acid (MCPA) counteracted the improving effect of mannuronate oligosaccharides (MAOS) in aging mice. (A) Butyrate level. (B–D) Relative protein levels of PPARα (B), AMPK (C), and HIF-1α (D) protein productions were normalized to glyceraldehyde-3-phosphate dehydrogenase (GAPDH) using Western bloting. (E) Immunohistochemical staining in ZO-1. (F) Integral optical density (IOD) of ZO-1. (G) Intestinal permeability in fecal microbiota transplantation (FMT) from control (CON) group (F-CON), FMT from aging group (F-aging), and FMT from aging + MAOS group (F-AM), respectively. (H, I) Transmission electron microscopy (TEM) observation of dermal-epidermal junction (DEJ) structure in back skin (H); and DEJ convolution (I); (J) TEM observations of mitochondria. (K) Reactive oxygen species (ROS) were measured by enzyme-linked immunosorbent assay (ELISA). (L–O) Relative protein levels of PINK1 (L), Parkin (M), VDAC1 (N), and Mfn2 (O) protein productions were normalized to GAPDH using Western bloting in skin of CON, aging, aging + MAOS, and aging + MAOS + MCPA (AMM) groups, respectively. The mice in F-CON, F-aging, and F-AM groups are 2 months; CON: 8 months; aging: 12 months; aging + MAOS: 12 months; and AMM: 12 months. Values are presented as the means ± standard deviation. Differences were assessed by analysis of variance (ANOVA) and denoted as follows: $^{*}P < 0.05$, $^{\#}P < 0.01$, and $^{\&}P > 0.05$, compared to F-aging/aging group.

3.7. FMT rebuilt the skin status similar to CON, aging, and aging + MAOS mice

The intestinal microbiota disorder, a pathological status called intestinal microbiota disorder, plays a negative influence on skin structure and integrity in aging mice. Therefore, we further proved the connection between intestinal microbiota and skin homeostasis and the improvement effect of MAOS on it using FMT experiment (Fig. 8). Our data indicated the value of DEJ and contents of collagen IV, COL17A1, and Laminin 311 proteins decreased significantly in the skin of F-aging mice compared with F-CON group (Figs. 8A–F). Moreover, there also were mitochondrial dysfunction in F-aging mice, as evidenced by altered mitochondrial morphology, decreased levels in mtDNA and ATP, and increased levels in ROS and Caspase-3 protein (Figs. 8G–L) versus F-CON group. Furthermore, the contents of HDAC3 and PHD proteins significantly increased, while the contents of pVHL, HIF-1α, PINK1, Parkin, VDAC1, and Mfn2 proteins obviously decreased (Figs. 8M–T), indicating there was a downregulation of mitophagy level in F-aging mice compared with F-CON group. Whereas, there was no remarkable difference in these indices between F-CON and F-AM groups, further highlighting the improvement effect of MAOS. Studies also have indicated that functional oligosaccharides are beneficial to gut homeostasis via regulating the intestinal microbiota, such as fructooligosaccharides, galactooligosaccharides, and chitooligosaccharides [34]. Notably, in the colon of mice in F-CON group, the levels of butyrate, PPARα, AMPK, HIF-1α, and ZO-1 proteins significantly decreased, while the intestinal permeability significantly increased (Figs. 9A–G), suggesting HIF-1α-related regulatory function impaired in the intestine of F-aging group compared with F-CON group. As a major source of energy in the large intestine, butyrate is involved in oxidative phosphorylation, consuming oxygen to produce ATP, supplying energy to cells, and causing intestinal hypoxia [35,36]. HIF-1α mediates the adaptation of intestinal cells to hypoxia and is important for maintaining the gut barrier, removing pathogenic material, and regulating mucin production and cellular energy [37]. Moreover, butyrate can maintain intestinal homeostasis via mediating HIF-1α stability [38]. Therefore, butyrate-HIF-1α axis is critical for intestinal homeostasis.

These results revealed that the intestinal microbiota disturbance, especially the reduction of butyrate content, induced the gut-skin axis dysregulation, ultimately leading to skin aging in mice, while MAOS supplementation exerted an improvement effect on it.

3.8. MCPA counteracted the improving effect of MAOS in aging mice

Research has proved that the HIF-1α-mediated mitophagy pathway inhibits osteosarcoma metastasis [39]. Moreover, butyrate, an HDAC3 antagonist, upregulated HIF in epithelial cell lines [40]. Meanwhile, exogenous supplementation of butyrate may also promote the stability of HIF-1α via inhibiting PHD expression [41]. To further validate that MAOS mediates an increase in butyrate content to improve skin aging, we established a MAOS supplied natural aging mouse model with or without MCPA-supplied. MCPA can irreversibly suppress SCFA acyl-CoA dehydrogenases, especially butyryl-CoA dehydrogenase, thereby blocking the β-oxidation of butyrate [11]. MCPA has been proved to irreversibly suppress the metabolism of butyrate and decrease acetyl-CoA content by 70%–90% in rat hepatocytes [12]. Our results indicated that MCPA could counteract the improvement effect of MAOS and induced a DEJ decrease and mitochondrial structural damage and an increase of ROS level in the skin in AMM group, compared with aging + MAOS group (Figs. 9H–K), indicating that MAOS-mediated butyrate obviously ameliorated skin aging and skin apoptosis response in mice. In addition, mitophagy levels in the skin of AMM mice were significantly decreased, as evidenced by the obvious downregulation in the contents of PINK1, Parkin, VDAC1, and Mfn2 proteins versus aging + MAOS mice (Figs. 9L–O), indicating that MAOS-mediated butyrate content exerts a positive effect on the aging-induced decrease in mitophagy level in the skin.

Overall, the ameliorative effect of MAOS disappeared when the MAOS supplementation was accompanied by the administration of MCPA by enema, thereby inhibiting the β-oxidation of butyrate in the intestine, indicating that MAOS-mediated butyrate consumes oxygen in the intestine through β-oxidation to activate HIF-1α in the intestine to maintain intestinal homeostasis, and ultimately improve skin aging.

4. Conclusion

Our study suggests that the MAOS-mediated intestinal butyrate-HIF-1α axis restored intestinal homeostasis, further increased HIF-1α-regulated mitophagy level in the skin, and ultimately improved skin aging in mice. This study clearly confirmed, with original evidence, the positive effect of MAOS as a physical moderator of the gut-skin axis and supported the recent expansion of the definition of psychobiotics to include MAOS-based techniques.

CRediT author statement

Ting Gao: Conceptualization, Methodology, Formal analysis, Writing - Original draft preparation, Visualization, Methodology; **Yixuan Li:** Formal analysis, Resources, Supervision, Project administration, Funding acquisition; **Xiaoyu Wang:** Methodology, Visualization; **Fazheng Ren:** Conceptualization, Formal analysis, Validation, Writing - Reviewing and Editing, Project administration, Funding acquisition, Supervision.

Declaration of competing interest

The authors declare that there are no conflicts of interest.

Appendix A. Supplementary data

Supplementary data to this article can be found online at https://doi.org/10.1016/j.jpha.2023.12.001.

References

[1] A. Jabłońska-Trypuć, R. Krętowski, M. Kalinowska, et al., Possible mechanisms of the prevention of doxorubicin toxicity by cichoric acid-antioxidant nutrient, Nutrients 10 (2018), 44.
[2] E.A. Grice, J.A. Segre, The skin microbiome, Nat. Rev. Microbiol. 9 (2011) 244–253.
[3] M. Boer, E. Duchnik, R. Maleszka, et al., Structural and biophysical characteristics of human skin in maintaining proper epidermal barrier function, Postepy Dermatol. Alergol. 33 (2016) 1–5.
[4] P. Zhang, J. Liu, B. Xiong, et al., Microbiota from alginate oligosaccharide-dosed mice successfully mitigated small intestinal mucositis, Microbiome 8 (2020), 112.
[5] D. Cheng, C. Jiang, J. Xu, et al., Characteristics and applications of alginate lyases: A review, Int. J. Biol. Macromol. 164 (2020) 1304–1320.
[6] S. Lu, K. Na, J. Wei, et al., Alginate oligosaccharides: The structure-function relationships and the directional preparation for application, Carbohydr. Polym. 284 (2022), 119225.
[7] S. Tajima, H. Inoue, A. Kawada, et al., Alginate oligosaccharides modulate cell morphology, cell proliferation and collagen expression in human skin fibroblasts *in vitro*, Arch. Dermatol. Res. 291 (1999) 432–436.
[8] G. Chen, Z. Chen, X. Fan, et al., Gut-brain-skin axis in psoriasis: A review, Dermatol. Ther. 11 (2021) 25–38.
[9] M. Szántó, A. Dózsa, D. Antal, et al., Targeting the gut-skin axis - Probiotics as new tools for skin disorder management? Exp. Dermatol. 28 (2019) 1210–1218.

[10] S. Lu, K. Na, J. Wei, et al., Alginate oligosaccharide structures differentially affect DSS-induced colitis in mice by modulating gut microbiota, Carbohydr. Polym. 312 (2023), 120806.
[11] E.A. Kean, Selective inhibition of acyl-CoA dehydrogenases by a metabolite of hypoglycin, Biochim. Biophys. Acta 422 (1976) 8–14.
[12] Y.K. Lieu, B.Y. Hsu, W.A. Price, et al., Carnitine effects on coenzyme A profiles in rat liver with hypoglycin inhibition of multiple dehydrogenases, Am. J. Physiol. 272 (1997) E359–E366.
[13] D. Harman, The biologic clock: The mitochondria? J. Am. Geriatr. Soc. 20 (1972) 145–147.
[14] A.T. Slominski, R. Hardeland, M.A. Zmijewski, et al., Melatonin: A cutaneous perspective on its production, metabolism, and functions, J. Invest. Dermatol. 138 (2018) 490–499.
[15] I. Rusanova, L. Martínez-Ruiz, J. Florido, et al., Protective effects of melatonin on the skin: Future perspectives, Int. J. Mol. Sci. 20 (2019), 4948.
[16] J.W. Doyle, T.P. Roth, R.M. Smith, et al., Effects of calcium alginate on cellular wound healing processes modeled *in vitro*, J. Biomed. Mater. Res. 32 (1996) 561–568.
[17] A. Kawada, N. Hiura, M. Shiraiwa, et al., Stimulation of human keratinocyte growth by alginate oligosaccharides, a possible co-factor for epidermal growth factor in cell culture, FEBS Lett. 408 (1997) 43–46.
[18] A. Sreedhar, L. Aguilera-Aguirre, K.K. Singh, Mitochondria in skin health, aging, and disease, Cell Death Dis. 11 (2020), 444.
[19] G. Lenaz, Mitochondria and reactive oxygen species. Which role in physiology and pathology? Adv. Exp. Med. Biol. 942 (2012) 93–136.
[20] H.R. Griffiths, D. Gao, C. Pararasa, Redox regulation in metabolic programming and inflammation, Redox Biol. 12 (2017) 50–57.
[21] M.Z. Springer, K.F. MacLeod, In Brief: Mitophagy: Mechanisms and role in human disease, J. Pathol. 240 (2016) 253–255.
[22] E. Lionaki, M. Markaki, K. Palikaras, et al., Mitochondria, autophagy and age-associated neurodegenerative diseases: New insights into a complex interplay, Biochim. Biophys. Acta 1847 (2015) 1412–1423.
[23] S. Von Stockum, A. Nardin, E. Schrepfer, et al., Mitochondrial dynamics and mitophagy in Parkinson's disease: A fly point of view, Neurobiol. Dis. 90 (2016) 58–67.
[24] H.J. Kim, S.H. Lee, S.J. Hong, Antibiotics-induced dysbiosis of intestinal microbiota aggravates atopic dermatitis in mice by altered short-chain fatty acids, Allergy Asthma Immunol. Res. 12 (2020) 137–148.
[25] B. Polkowska-Pruszyńska, A. Gerkowicz, D. Krasowska, The gut microbiome alterations in allergic and inflammatory skin diseases - an update, J. Eur. Acad. Dermatol. Venereol. 34 (2020) 455–464.
[26] V.A. Poroyko, A. Carreras, A. Khalyfa, et al., Chronic sleep disruption alters gut microbiota, induces systemic and adipose tissue inflammation and insulin resistance in mice, Sci. Rep. 6 (2016), 35405.
[27] Y. Belkaid, J.A. Segre, Dialogue between skin microbiota and immunity, Science 346 (2014) 954–959.
[28] B. De Pessemier, L. Grine, M. Debaere, et al., Gut-skin axis: Current knowledge of the interrelationship between microbial dysbiosis and skin conditions, Microorganisms 9 (2021), 353.
[29] L.F. Dawson, E.H. Donahue, S.T. Cartman, et al., The analysis of para-cresol production and tolerance in *Clostridium* difficile 027 and 012 strains, BMC Microbiol. 11 (2011), 86.
[30] K. Miyazaki, N. Masuoka, M. Kano, et al., *Bifidobacterium* fermented milk and galacto-oligosaccharides lead to improved skin health by decreasing phenols production by gut microbiota, Benef. Microbes 5 (2014) 121–128.
[31] J.L. Boyajian, M. Ghebretatios, S. Schaly, et al., Microbiome and human aging: Probiotic and prebiotic potentials in longevity, skin health and cellular senescence, Nutrients 13 (2021), 4550.
[32] X. Ai, P. Yu, L. Luo, et al., *Berberis dictyophylla* F. inhibits angiogenesis and apoptosis of diabetic retinopathy via suppressing HIF-1α/VEGF/DLL-4/Notch-1 pathway, J. Ethnopharmacol. 296 (2022), 115453.
[33] Q. Lin, S. Li, N. Jiang, et al., Inhibiting NLRP3 inflammasome attenuates apoptosis in contrast-induced acute kidney injury through the upregulation of HIF1A and BNIP3-mediated mitophagy, Autophagy 17 (2021) 2975–2990.
[34] N. Liu, H. Wang, Z. Yang, et al., The role of functional oligosaccharides as prebiotics in ulcerative colitis, Food Funct. 13 (2022) 6875–6893.
[35] J. Karhausen, V.H. Haase, S.P. Colgan, Inflammatory hypoxia: Role of hypoxia-inducible factor, Cell Cycle 4 (2005) 256–258.
[36] Š. Konjar, M. Pavšič, M. Veldhoen, Regulation of oxygen homeostasis at the intestinal epithelial barrier site, Int. J. Mol. Sci. 22 (2021), 9170.
[37] R. Singhal, Y.M. Shah, Oxygen battle in the gut: Hypoxia and hypoxia-inducible factors in metabolic and inflammatory responses in the intestine, J. Biol. Chem. 295 (2020) 10493–10505.
[38] J.L. Fachi, J. de Souza Felipe, L.P. Pral, et al., Butyrate protects mice from *Clostridium* difficile-induced colitis through an HIF-1-dependent mechanism, Cell Rep. 27 (2019) 750–761.e7.
[39] G. He, J. Nie, X. Liu, et al., Zinc oxide nanoparticles inhibit osteosarcoma metastasis by downregulating β-catenin via HIF-1α/$BNIP_3$/LC3B-mediated mitophagy pathway, Bioact. Mater. 19 (2023) 690–702.
[40] C.J. Kelly, L. Zheng, E.L. Campbell, et al., Crosstalk between microbiota-derived short-chain fatty acids and intestinal epithelial HIF augments tissue barrier function, Cell Host Microbe 17 (2015) 662–671.
[41] R.X. Wang, M.A. Henen, J.S. Lee, et al., Microbiota-derived butyrate is an endogenous HIF prolyl hydroxylase inhibitor, Gut Microbes 13 (2021), 1938380.